Draft version January 12, 2021
Typeset using LaTeX **twocolumn** style in AASTeX63

Searching For Transiting Planets Around Halo Stars. II. Constraining the Occurrence Rate of Hot Jupiters

Kiersten Boley,[1] Ji Wang (王吉),[1] Joel Zinn,[1,2] Karen A. Collins,[3] and Tianjun Gan[4]

[1] *Department of Astronomy, The Ohio State University, Columbus, OH 43210*
[2] *Department of Astrophysics, American Museum of Natural History, Central Park West at 79th Street, NY 10024, USA*
[3] *Center for Astrophysics | Harvard & Smithsonian, 60 Garden Street, Cambridge, MA 02138, USA*
[4] *Department of Astronomy and Tsinghua Centre for Astrophysics, Tsinghua University, Beijing 100084, Chin*

ABSTRACT

We present an improved estimate of the occurrence rate of hot Jupiters orbiting metal-poor dwarfs with -2.0 $\leq$ [Fe/H] $\leq$ -0.6 by searching 11,125 halo stars observed with TESS for transiting planets. We evaluate the sensitivity of our detection pipeline by conducting an extensive injection-recovery tests. In total, we inject 2,225,000 transit signals (200 injections per star). We use and compare two different transit search algorithms: Transit Least Squares (TLS) and Box Least Squares (BLS) and find no significant difference between the two algorithms. Within our sample, we do not detect any hot Jupiters. Using the binomial distribution, we place the most stringent upper limit on hot Jupiter occurrence around metal-poor stars. We find a 1-σ upper limit HJ occurrence to range between $0.05\% \leq f_p \leq 0.36\%$ for each bin with the mean occurrence 0.19 % for radii 0.8 -2 $R_{\rm Jupiter}$ and periods $0.5 - 10$ days.

Keywords: exoplanets, TESS, planet, occurrence

1. INTRODUCTION

The evolution of the Milky Way and planet formation are interconnected (Forgan et al. 2017). Metallicity links these seemingly unrelated topics by playing an important role in the formation and evolution of stars, and therefore affects the formation of planets (Johnson & Apps 2009; Choi & Nagamine 2009). Host star metallicity is thought to reflect the metallicity of the protoplanetary disk from which planets form (Wyatt et al. 2007; Haworth et al. 2016). Given that the first generation of stars were metal-poor, the first planets must also be lacking in metals. By probing planet occurrence in the metal-poor regime, we can gain insight into the first planet formation and determine the metallicity at which no planet can form.

A metal-poor environment poses many challenges for planet formation. At low metallicity, the protoplanetary disk lifetime is significantly shorter decreasing the likelihood of planet formation (Kornet et al. 2005; Yasui et al. 2010; Ercolano & Clarke 2010). The vast majority of the gas is hydrogen and helium, and heavy elements compose only a fraction $\sim 10^{-5}$ of the total mass within the metal-poor regime (Johnson & Li 2012). This effect can be especially detrimental at short orbital distances where planet formation is thought to be dominated by core accretion (Miller & Fortney 2011; Bailey & Batygin 2018). Although the planet formation is increasingly improbable with decreasing metallicity, the dependence of Jovian planet formation on metallicity is well-known.

Since the discovery of four Jovian planets orbiting metal-rich stars in 1997 by Gonzalez et al. (2001), the correlation between planet occurrence and host star metallicity has been a point of focus within the exoplanet community. Following this discovery, various studies also noted that Jovian planets preferentially orbit metal-rich stars (Santos et al. 2004; Fischer & Valenti 2005; Mortier et al. 2013). The occurrence of Jovian planets is shown to increase exponentially with the increase of metallicity for solar and super-solar metallicities (Udry & Santos 2007; Johnson et al. 2010; Mortier et al. 2013); however, the hot Jupiter (HJ) occurrence trend within the metal-poor regime is still uncertain. Using radial velocities, Sozzetti et al. (2009) and Mortier et al. (2012) probed this regime to determine Jovian planet occurrence and provide an upper limit for hot Jupiter occurrence in the metal-poor regime. Since the

boley.62@osu.edu

study conducted by Mortier et al. (2012), there has been little investigation to further constrain hot Jupiter planet occurrence in at low metallicities.

With advent of Transiting Exoplanet Survey Satellite (TESS) (Ricker et al. 2015), it is the opportune time to revisit HJ occurrence in the metal-poor regime as TESS provides many advantages compared to Kepler to complete this work. While the Kepler mission could have conducted a search for giant planets around halo stars, the mission was primarily focused on the detection of smaller planets; therefore, FGK stars were predominately observed. Similarly, TESS is also focused on searching for small planets around bright stars. The advantage of TESS is it's larger field of view which allows for 30-minute cadence Full Frame Images (FFI). These FFIs provide observations of a wide range of stellar types. TESS also covers $\sim 85\%$ of the sky, which is a significant improvement to the $\sim 0.25\%$ monitored by Kepler. Given the capabilities and mission of Kepler, it is unsurprising that a more robust determination of the HJ occurrence within the metal-poor regime has not occurred until now.

In this paper, we focus on further constraining hot Jupiter planet occurrence in the metal-poor regime (-2.0 $\leq$ [Fe/H] $\leq$ -0.6) using a population of halo stars, as they provide important insights into planet-formation processes in the first generation of stars within the Milky Way. Our approach to deriving hot Jupiter occurrence rates is largely inspired by the method first outlined by Dressing & Charbonneau (2015). We perform a full transit search of our sub-dwarf sample, using both the box least squares algorithm (Kovács et al. 2002) and Transit Least Squares (Hippke & Heller 2019) to search the light curves. Using an injection-recovery scheme to calculate our detection sensitivity, we use our results to constrain the occurrence rate of hot Jupiters orbiting halo stars.

The outline of our paper is as follows. Section 2 provides a description of our stellar sample. In Section 3, we discuss the method from which we acquire TESS data. We explain our planet detection pipeline in Section 4. Section 5 contains a description of our planet injection pipeline. In Section 6, we assess the completeness of our pipeline. Section 7 is dedicated to a statistical analysis of the data and estimation of the planet occurrence rate. We compare our results to previous studies in Section 8 and their implications for the frequency of hot Jupiters in the metal-poor regime before concluding in Section 9.

2. STELLAR SAMPLE

We selected ~16,940 halo sub-dwarfs for the search for HJs using TESS data. Details on the sample selection and validation can be found in a companion paper (Kolecki et al. 2020). We briefly describe the sample selection here. The sample is selected by using two sources of complementary information: (1) the full, 3D kinematic information and (2) the transverse kinematic information. The former was constructed following Koppelman et al. (2018), using radial velocities as well as proper motions from Gaia DR2 (Gaia Collaboration et al. 2018) to select stars within 1 Kpc and with 3D velocities greater than 210 km/s with respect to the local standard of rest. The latter sample was chosen using heuristic tangential motion cuts based on simulations of the Milky Way from Galaxia (Sharma et al. 2011). By checking with APOGEE spectra, we confirmed that 70% of selected targets are genuine halo stars. A H-R diagram of the sample is provided in Fig. 1. The discontinuity in the distribution is due to the inhomogeneous treatment to low-mass stars and other stars in the TESS Input Catalog (see Appendix E.1.1 in Stassun et al. 2018).

Roughly 65% (11,125 out of 16,940) of the sample was observed by TESS through sector 23 (Ricker et al. 2015). Only a small fraction (add percentage here) of the sample had TESS 2-min cadence data, resulting a small usable sample. To take advantage of a bigger sample, we obtained 30-min-cadence light curves using TESS Full Frame Images (FFI) with `Eleanor` (Feinstein et al. 2019). The FFI light curves are then used for planet detection and injection-recovery tests.

3. ACQUIRING TESS DATA

With `Eleanor`, we download 30-min-cadence TESS FFIs. Using the T_{mag} of each target, we determine the optimal aperture size, which is then input into Eleanor. We download the four different data files: "PCA", "Correlated", "Raw", and "PSF". From there, we determine the noise level of each light curve. We normalize the flux data by the dividing the light curve by the median flux. The noise of each file is determined by calculating the RMS noise of the light curve. The data file with the least amount of noise is saved.

4. PLANET DETECTION PIPELINE AND RESULTS

To determine the occurrence rates and completeness of our search, we must search within our sample for planet candidates. We developed an automated pipeline that encompasses all the data processing to include detrending, noise removal, and transit search. Given that our target stars are relatively faint, we must maximize the quality of our data. As this pipeline is used for millions of transit searches, we make every effort to be computationally efficient.

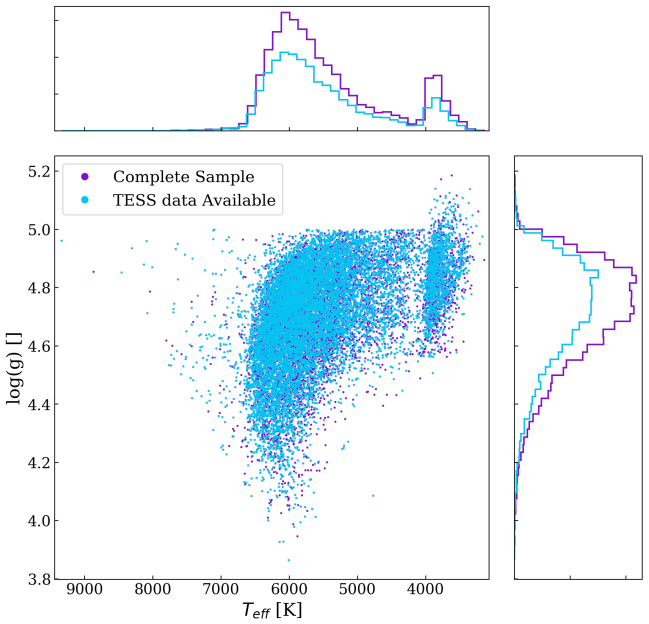

Figure 1. surface gravity and stellar effective temperatures of the stars in our final sample (cyan) compared to the complete sample (purple) initially selected based on kinematic information. The bump at low mass and and radius is most likely from these stars being a cool dwarf.

We begin by detrending the light curves. The data is initially detrended using `Wotan` (Hippke et al. (2019)) with the Turkish bi-weight method, which is indicated to be the most robust detrending method. Since the TESS data has sharp peaks at the beginning and ends of an observation, we perform sigma-clipping to remove any systematics that wotan was unable to remove. We determine the outliers at the edges of the light curves and at the edges of the data gaps. We consider 5% of the points on the edges of the data gaps. We calculate the median of the complete light curve any points that are over 3σ are removed from the data. From here our pipeline splits into two separate transit search algorithms: Transit Least Squares (TLS, Hippke & Heller 2019)) and a box least squares alogorithm (BLS, Kovács et al. 2002)).

TLS, an open source transit search python package, is noted to be more efficient at conducting transit searches for small planets. We were interested in whether it also performs better than BLS for giant planets. To test how well TLS performs, we used the default transit template along with all the default options. We also made use of the box template for comparison purposes as well.

For our BLS algorithm, we used the reference implementation of BLS provided by `astropy 4.0.1` (Astropy Collaboration et al. 2013). With this implementation, the stochastic differential equation (SDE), false alarm probability (FAP), and signal to noise ratio (SNR) are not provided; however, they are required within the vetting process. In Section 4.1, we expand upon how we calculate the SDE, FAP, and SNR given that these values are not calculated by the BLS program that we employed.

4.1. *BLS*

Given our choice to use two transit search algorithms, we make every effort to conduct a fair comparison. TLS outputs SDE opposed to the implementation of BLS that we use in this study. The `astropy` implementation is output in terms of log-likelihood; therefore, we must convert log-likelihood to χ^2 to determine the SDE for a given light curve. χ^2 is related to the log-likelihood by

$$\chi^2 = -2\ ln\mathcal{L} + C \tag{1}$$

where $\mathcal{L}$ is the likelihood and C is a constant. Similar to TLS (Hippke & Heller 2019), we calculate the signal residual as

$$SR(P) = \frac{-2\ ln\mathcal{L}_{min} + C}{-2\ ln\mathcal{L}(P) + C} = \frac{\chi^2_{min}}{\chi^2(P)} \tag{2}$$

Using the SR, we can then determine the SDE as described in Kovács et al. (2002) and Hippke & Heller (2019).

$$SDE = \frac{SR_{peak} - \langle SR(P)\rangle}{\sigma(SR(P))} \tag{3}$$

where SR_{peak} is the peak value of SR(P), $\langle SR(P)\rangle$ is the mean of SR(P), and $\sigma(SR(P))$ is the standard deviation.

From the SDE, we use the FAP value table from TLS to determine the FAP value for BLS. Using the TLS conversion table, we can maintain a consistent comparison between both algorithms. Their conversion table was constructed from an experiment with >10000 white noise-only TLS search runs, which maps SDE to a particular FAP value (e.g. SDE=7 corresponds to 1-FAP=0.99).

Within BLS, the signal-to-noise ratio (SNR) is not automatically determined; therefore, we calculate a SNR for each fit as

$$SNR = \frac{d}{\sigma}\sqrt{n_{transit}} \tag{4}$$

where d is the difference between the median of the data points in the transit and the flux level outside the transit, $n_{transit}$ is the number of points within transit, and σ is the the sigma-clipped standard deviation of the detrended lightcurve.

4.2. *Vetting*

Using our transit detection pipeline, we identified 2128 transit events with SNR greater than 5σ. Some of those signals might have been systematics or astrophysical false positives instead of transiting planet candidates. Therefore, we conducted a series of cuts to select the events consistent with transiting planets, which is described below.

After the light curves are searched using either TLS or BLS, any potential detections are sent through `Edivetter Unplugged` (Zink et al. 2020) to vet the lightcurves. With `Edivetter Unplugged`, we cut all events that with transits that are not unique and for secondary eclipses. From this cut, we had 311 transit events remaining. We then remove any detections with an FAP value to be ≤ 0.0001. Next, we conducted a visual examination for the remaining candidate events. We checked for the appearance of secondary eclipses and considered the depth of the transit relative to other potential features. We rejected the 309 signals with 2 remaining transit signals. The rejected signals were determined to be either eclipsing binaries, systematic, or sinusoidal brightness variations indicative of starspots.

4.3. *Follow-up observations & Results*

The two candidates that survived our vetting process and continued on to follow-up observations are TIC 229802010 and TIC 188593929. For TIC 229802010, we took one high-resolution spectrum using the MIKE spectrograph on the Magellan telescope on UT Jul 27 2019 (PI: Ting Li). This spectrum had an exposure time of 1500 seconds resulting in a SNR of 10 per pixel; therefore, providing a sufficient SNR to cross-correlate a solar-type synthetic spectrum with the observed spectrum. The cross-correlation function clearly showed double peaks that were separated by ∼50 km/s, which is indicative of a grazing eclipsing binary (EB) system.

Within the TESS follow-up observation collaboration, we took two RV data points with CHIRON (Tokovinin et al. 2013) at a phase of approximately 0.45 and 0.82 (PI: Samuel Quinn). However, the RV data quality was insufficient to conclusively rule out the EB scenario. Ground-based photometry later retired TIC 188593930 as a false positive because a deep eclipse was observed on a nearby faint star TIC 188593929 [1]. Therefore, we find that none of the light curves in our sample to exhibit light curves indicative of a Jovian transiting planet.

5. PLANET INJECTION PIPELINE

In order to accurately measure the planet occurrence rate based on the results of our planet search, we need to determine the probability of detecting a planet using our pipeline. We measure the detection sensitivity of our planet detection pipeline by injecting transiting planets into the TESS light curves, and running the light curves through our detection pipeline where they will be detrended and vetted. We generate synthetic transit signals for each light curve with orbital parameters drawn from a uniform distribution using pylightcurve (Tsiaras et al. 2016). Each synthetic planet signal that is injected into a light curve has a randomly determined planetary radius, orbital period, inclination and eccentricity (Rp, P, i, e) taken from the following uniform distributions:

$$\frac{P}{day} \sim U(0.5, 20)$$

$$\frac{R_p}{R_j} \sim U(0.08, 2)$$

$$t_0 \sim U(0, P)$$

$$i \sim U(i_{min}, i_{max})$$

where i_{max} and i_{min} are calculated for each star as the maximum and minimum inclination for a transit using the semi-major axis and the radius each star. The eccentricity is set to 0, given that hot Jupiters are subject to strong orbital circularization and are expected to typically have low eccentricities (e.g., Alvarado-Montes & García-Carmona 2019). Using the stellar parameters, the limb darkening parameters estimated from the coefficients in Claret & Bloemen (2011). Each modified light curve containing a synthetic planet signal is then sent through our planet detection pipeline.

For a synthetic planet signal to be considered a detection, we used a nearly identical vetting process to the detection pipeline. We require the SNR to be greater than 5σ. The modified light curves must be determined by `Edivetter Unplugged` not to be a false positive. We also require the FAP value to be ≤ 0.0001, which corresponds to an SDE=9.1. After the modified light curve undergoes this vetting process, the remaining synthetic planet signals are considered a detection if the detected period of the planet matches to within 10% of the generated period. Period aliases of the injected signal are not treated as detections. It is important to note that unlike real data, we do not conduct visual inspections as it would be highly impractical given the large number of injections.

5.1. *Assessing our Pipeline*

[1] https://exofop.ipac.caltech.edu/

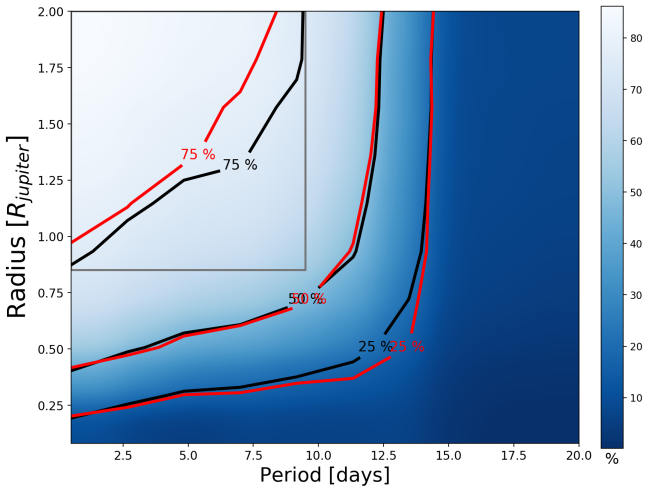

Figure 2. Smoothed map comparing the detection sensitivity of BLS (Black) to TLS (Red). As indicated in the color bars, darker regions correspond to lower detection efficiency. The grey box indicates the region 0.85-2 R_p and 0.5-9.5 days where TLS performs worse than BLS.

To assess the detection sensitivity of our pipeline, we conducted an extensive injection-recovery tests. For each star, we generated 200 synthetic transit signals per light curve. In total, we injected 2,225,000 transiting planets into the light curves of the 11,125 stars for both TLS and BLS. Our pipeline successfully recovered ∼80% of injected planet signals with a SNR $\geq$ 10 within the range of $0.8-2$ R_J and periods $0.5-10$ days using BLS. We used both TLS and BLS and compare their results; however, we use only the results from BLS in Figure 3.

We calculate the detection sensitivity by dividing the number of the synthetic planet signals detected by the total planet signals injected. We take this fraction as the detection sensitivity, which is binned as a function of planet period and radius. As shown in Figure 2 , we found that our pipeline is sensitive to injected planets with radii larger than 0.85 R_j. Most of those planets signals were detected with nearly 75% efficiency out to the orbital period of $\sim$ 9.5 days. Our pipeline displayed a significant decrease in the detection sensitivity of planets with radii $<$ 0.5 R_j with the recovery fraction $\sim$ 19% and 0.5-2.0 R_j planets with periods longer than 9.5 days with the recovery fraction ∼11.5%; however, the decrease in detection sensitivity for smaller planets and longer periods does not significantly affect our ability to constrain the occurrence rate for hot Jupiters.

5.2. *Comparison of TLS vs BLS*

Although the BLS algorithm has become a standard tool for transit searches, Hippke & Heller (2019) developed a new planet transit search algorithm, TLS, which is optimized to detect small planets. Instead of a box-shaped template, they use a template based on actual transiting planets. Given our large data set, we determined that it would be pragmatic to compare TLS and BLS for hot Jupiters.

As stated in Section 4, our detection pipeline allows us to run TLS or BLS. During our planet injection-recovery tests, we save the modified light curves, which are then sent through both TLS and BLS ensuring an impartial comparison. For TLS, we use the default template for the first set of 2,225,000 injections and conduct a second set of injections using the box template.

In Figure 2, we show the detection sensitivity. We find that overall TLS successfully recovered 38.4% of the injected planets using the default template, while BLS successully recovered 38.8%. However, within the region 0.85-2 R_p and 0.5-9.5 days BLS does slightly better and recovers 77.7% of the injected planets whereas TLS recovers 75.4%. Outside this region in higher period and lower radius, we find that TLS performs slightly better than BLS recovering 45.7 % and BLS recovering 45.1 %

We find that these algorithms are comparable for lower radius and larger period; however, BLS outperforms the default TLS options at short period and large radius. This difference in performance likely due to only selecting the default options for TLS as TLS under-performs BLS using the box template as well. TLS is versatile with many options the optimize the transit search for the particular type of planet in question; therefore, with the proper input TLS may have performed better than BLS. Adding these options can have computational costs, but for a smaller sample these would likely be worth including.

6. CALCULATING SEARCH COMPLETENESS

We define the search completeness to be the probability of finding a planet with a random orbital alignment within our sample using our detection pipeline. Therefore, the overall search completeness depends both on the detectability $P_{det}(R_p, P)$ of a particular transiting planet and the likelihood that a particular planet will be observed to transit. We determine the detection efficiency of our pipeline by conducting an extensive injection and recovery test using our planet injection pipeline (see Section 5).

Once the detection sensitivity was determined, we use the geometric transit probability to account for the likelihood of a planet being oriented so that a transit will be observed. For the geometric transit probability we assume an eccentricity of zero and use:

$$P_t(R_p, P) = \frac{R_p + R_\star}{a} \tag{5}$$

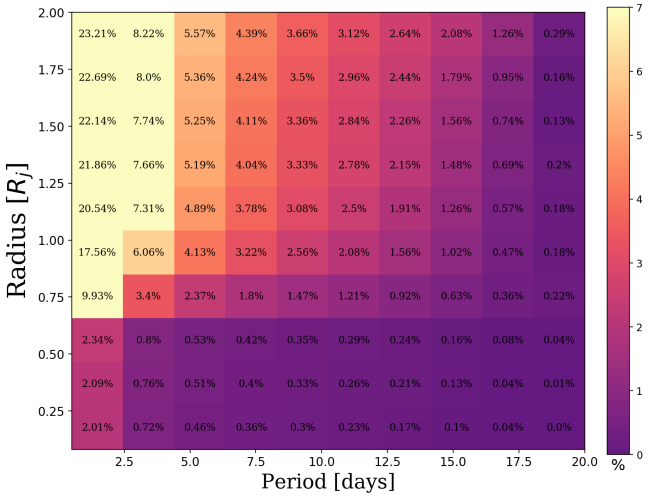

Figure 3. The search completeness using BLS, showing the probability of observing a planet with a random orbital alignment within our sample using our detection pipeline.

where $R_\star$ is the star radius and a the orbital semi-major axis. a is determined from Kepler' s third law assuming a stellar mass of $1.01 M_\odot$ and radius of $0.711 R_\odot$, which are the median values for the halo stars within our sample.

For a given orbital period, we computed the corresponding semimajor axis for a planet orbiting each of the stars in our sample. With the transit probability for each radius and orbital period, we calculated the search completeness by weighting the detection sensitivity by the geometric transit probability for each bin. In Figure 3, we show the search completeness.

7. PLANET OCCURRENCE RATE

To determine the upper limit of planet occurrence given a null detection, we follow the procedure originally described in the appendix of Burgasser et al. (2003) and McCarthy & Zuckerman (2004) using the binomial distribution. The probability $P(f_p)$ of finding d detections in a sample of size N can be calculated as a function of the true planet frequency f_p:

$$P(f_p) = f_p^d \ (1 - f_p)^{N-d} \ \frac{N-1}{(N-d)!\ d!} \tag{6}$$

In the case of a null detection d = 0, the maximum planet frequency can be solved for

$$f_{p,max} = 1 - (1 - P(f_p))^{\frac{1}{N-1}} \tag{7}$$

Therefore, we can calculate upper limit of f_p at a given confidence level by setting $P(f_p)$ to the corresponding probability for the confidence level of interest.

However, not all planets are detectable using the transit method and N must be replaced by the effective sample size N_{eff}. To calculate the true upper limit of planet occurrence, we must account for the geometric transit probability and the detection efficiency of our pipeline. Therefore, we define our effective sample size as:

$$N_{eff}(R_p, P) = N \times P_t(R_p, P) \times P_{det}(R_p, P) \tag{8}$$

where N is the total sample size, $P_t(R_p, P)$ is the geometric transit probability, $P_{det}(R_p, P)$ is the detection efficiency (see Section 6), P the orbital period and R_p the planet radius.

Using equation(7) and (8) , we calculate the the upper limit of hot Jupiter occurrence by measuring the range in f_p that covers 68% of the integrated probability function. This is equivalent to the 1-σ confidence level.

In Figure 4, we show the our results using the detection efficiency determined from BLS. For the upper limit of HJ occurrence, we consider a radius of $0.8 - 2\ R_J$ and periods $0.5 - 10$ days. We choose a radius of 2 R_J given that the majority of the confirmed planets to date are less than 2 R_J (Akeson et al. 2013). Within this region, we find upper limit of occurrence range between $0.05\% \leq f_p \leq 0.36\%$ within the parameter space considered with the mean upper limit of occurrence being $f_p < 0.19\%$.

8. COMPARISON TO PREVIOUS WORKS

The occurrence of hot Jupiters has been studied by multiple surveys. For HJs orbiting solar-type stars, RV surveys have found the occurrence to be between $0.9\% - 1.2\%$ (Wright et al. 2012; Marcy et al. 2005; Mayor et al. 2011; Petigura et al. 2018), which is in contrast to the significantly lower occurrence rates determined with transit surveys. The HJ occurrence observed using TESS and Kepler range between $0.4\% - 0.6\%$ (Howard et al. 2012; Fressin et al. 2013; Mulders et al. 2015; Santerne et al. 2016; Petigura et al. 2018; Zhou et al. 2019). Although TESS and Kepler observe different targets, the occurrence rates are consistent.

The difference in occurrence between RV and transit surveys may be attributed to the contamination of multiple stellar systems and evolved stars into the transit sample (Wang et al. 2015). Guo et al. (2017) investigated the differences in metallicity between Kepler and some radial velocity surveys; however, they found the difference in metallicity to be insufficient to explain the HJ occurrence discrepancy.

The first attempt to determine HJ occurrence within the metal-poor regime was Sozzetti et al. (2009). They

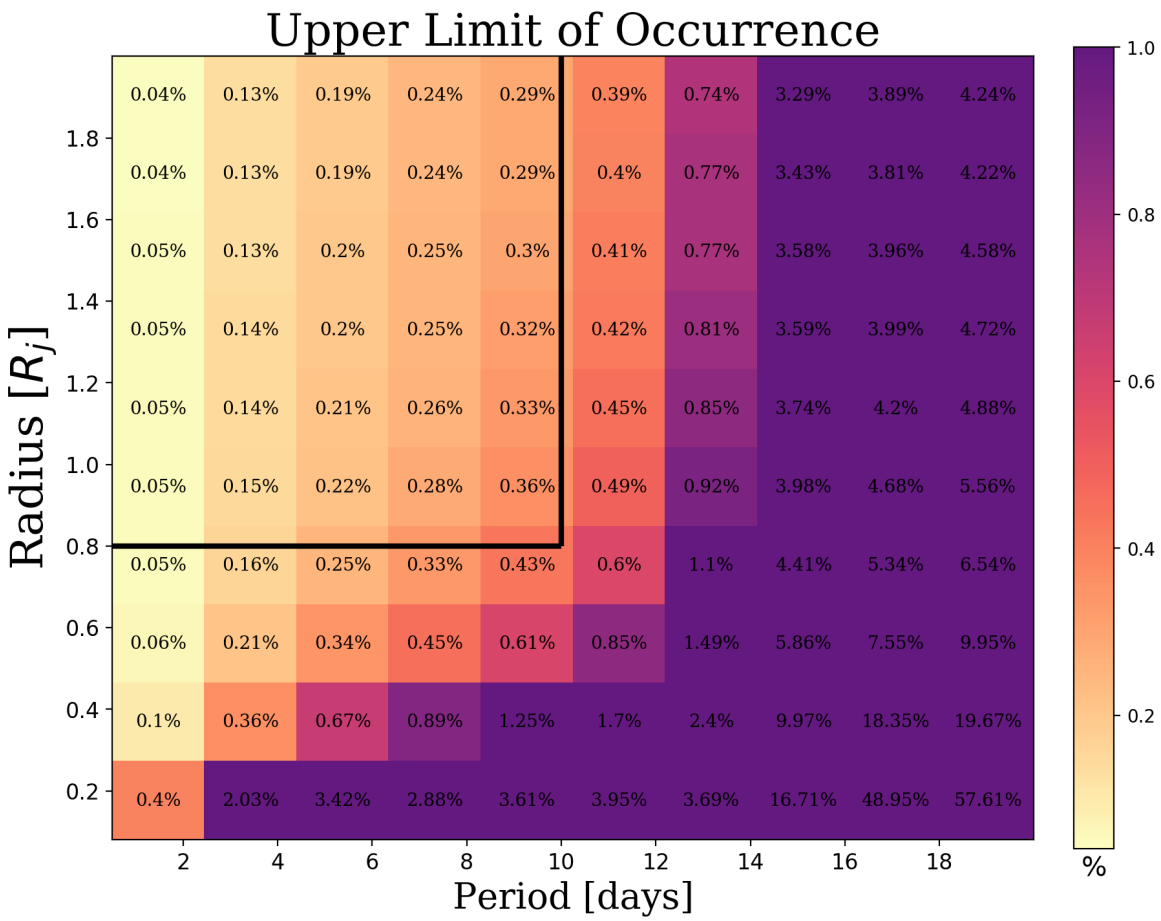

Figure 4. The region within the black box contains the binned upper limit of HJ occurrence within the metal-poor regime at the 1-σ confidence interval. The numbers within each grid cell indicate the upper limit of HJ occurrence rate as a percentage. We assume stellar mass of $1.01 M_{\odot}$ and radius of $0.711 R_{\odot}$.

used radial velocity data from HIRES on the Keck 1 telescope with a sample of 160 metal-poor stars. Consequently, strong constraints were derived for short-period gas giants where they had 95% completeness for periods ≤ 3 yrs with a minimum companion mass of $\sim 0.75\ M_J$, which corresponds to a HJ radius of approximately 1.25 R_J (Chen & Kipping 2017). Given that the majority of the range is for cool Jupiters, we consider radius as a step function using the Chen & Kipping (2017) for periods < 10 days and Thorngren et al. (2019) for periods > 10 days. Within the HJ range, we expect the planets to be inflated thereby increasing the radius. Their work resulted in a 1-σ upper limit of HJ occurrence of 0.67%.

The most recent work to directly consider this regime for HJs is Mortier et al. (2012). Similar to Sozzetti et al. (2009), radial velocity measurements were taken using HIRES and HARPS with a sample of 114 stars. The sample was restricted to targets that had six or more measurements. For a completeness of 80% and period < 10 days, they found a minimum companion mass of $\sim 0.314\ M_j$, which corresponds to a radius of 1.04 R_j (Chen & Kipping 2017). Once again, we use the Mass- Radius relationship from Chen & Kipping (2017) because we expect the HJs to be inflated. Given the smaller sample size, they found the 1-σ upper limit of HJ occurrence to be 1.00%.

Compared to the previous works using radial velocities, we place the most stringent upper limit on HJ occurrence. Using TESS data, we allow for a larger effective sample size that ranges from $N_{eff} = 313 - 2,582$ with a median of $N_{eff} = 576$. Our minimum effect sample size is $\sim 2-3$ times larger than the sample sizes of Mortier et al. (2012) and Sozzetti et al. (2009) (see Table 1). Another difference to note is that each study has varying ranges of radius and period (see Table 1); however, this does not significantly affect the comparison. For example, our upper limit of occurrence within the range Mortier et al. (2012) considered is between $0.05\% \leq f_p \leq 0.33\%$ with the mean upper limit of 0.19%.

Table 1. Hot Jupiter Occurrence Comparison

Author	N	f_p	Fe/H	P	R_p	Method
Petigura et al. (2018)	1883†	$0.57^{+0.14}_{-0.12}$%	(-0.5≤[Fe/H]≤ 0.5)	$1 \leq P \leq 10$ days	0.71-2.14R_j	Transit
Mayor et al. (2011)	822	0.9 ± 0.4%	(-0.5≤ [Fe/H] ≤ 0.5)	≤ 11 days	>0.75 R_j	RV
Masuda & Winn (2017)	1737†	$0.43^{+0.07}_{-0.06}$%	(-1≲ [Fe/H] ≲ 0.5)	$0.5 \leq P \leq 10$ days	0.8-2R_j	Transit
Wright et al. (2012)	836	1.2 ± 0.38%	(-1≤ [Fe/H] ≤ 0.5)***	≤ 10 days	>0.51R_j	RV
Zhou et al. (2019)	2401†	0.41 ± 0.10%	(-1≤[Fe/H]≤ 0.5)	$0.9 \leq P \leq 10$ days	0.8-2.5R_j	Transit
Mortier et al. (2012)	114	1.00%*	(-2.0≤ [Fe/H] ≤ 0)	≤ 10 days	>1.04 R_j	RV
Sozzetti et al. (2009)	160	0.67%*	(-2.0≤[Fe/H]≤ -0.6)	< 3 yrs	>1.25 R_j	RV
This Work	576†	0.19%*	(-2.0≤[Fe/H]≤ -0.6)	$0.5 \leq P \leq 10$ days	0.8-2R_j	Transit

NOTE— For all radial velocity surveys compared, we used the Chen & Kipping (2017) relation to convert from mass to radius.

† We estimate the median effective sample size using our detection sensitivity
* This is the maximum upper limit of occurrence

9. SUMMARY & CONCLUSIONS

In this paper, we presented an updated upper limit of HJ occurrence within the metal-poor regime using TESS data. We developed our own planet detection pipeline to search for transiting planets within our light curves. We then characterized the completeness of our pipeline by injecting simulated transiting planets into the light curves and attempting to recover them. Our search of the light curves of 11,125 halo stars revealed zero planet candidates. We then calculated the upper limit of occurrence HJs around halo stars by using the null detection hypotheses accounting for the geometric transit probability and the detection efficiency of our pipeline. The primary conclusions of this work are:

- In line with previous works, HJs are rare or non-existent in the metal-poor regime (-2.0 ≤ [Fe/H] ≤ -0.6).
- We further constrain the upper limit HJ occurrence within the metal-poor regime using TESS data. We find the upper limit of HJ occurrence range from 0.05% ≤ f_p ≤ 0.36% with the mean occurrence being f_p < 0.19% for radii 0.8 -2 R_j and periods $0.5 - 10$ days at the 1-σ confidence level, which places the most stringent constraint on HJ occurrence.
- TLS is comparable to the BLS when searching for HJs. It does slightly better that lower radius and high period; however, as radius and period increase BLS out-performs TLS.

Further constraining the occurrence of HJ occurrence would require significantly larger samples; however, any planet discoveries would be of great interest within the metal-poor regime. They would expand our knowledge on the environment in which the first generation of planets formed.

Moving forward, our future work will build upon this work. Using the framework that was developed conducting this study, we plan to determine an accurate functional form of planet occurrence vs. metallicity by constraining previous models (Johnson et al. 2010; Fischer & Valenti 2005; Udry & Santos 2007). We will consider a larger sample size and utilize the pipelines created for this work. This work acts as a starting point in constructing a galactic planet formation model, which relates the metal-enrichment of the Milky Way to planet formation.

ACKNOWLEDGMENTS

We would like to acknowledge Ben Montet and Adina Feinstein for their work in developing eleanor. We would also like to thank David Latham, Karen Collins, Sam Quinn, Tianjun Gan, Ting Li, Joanna Teske for conducting follow-up observations for our planet candidates.

REFERENCES

Akeson, R. L., Chen, X., Ciardi, D., et al. 2013, PASP, 125, 989, doi: 10.1086/672273

Alvarado-Montes, J. A., & García-Carmona, C. 2019, MNRAS, 486, 3963, doi: 10.1093/mnras/stz1081

Arriagada, P. 2011, ApJ, 734, 70, doi: 10.1088/0004-637X/734/1/70
Astropy Collaboration, Robitaille, T. P., Tollerud, E. J., et al. 2013, A&A, 558, A33, doi: 10.1051/0004-6361/201322068
Bailey, E., & Batygin, K. 2018, ApJL, 866, L2, doi: 10.3847/2041-8213/aade90
Burgasser, A. J., Kirkpatrick, J. D., Reid, I. N., et al. 2003, ApJ, 586, 512, doi: 10.1086/346263
Chen, J., & Kipping, D. 2017, ApJ, 834, 17, doi: 10.3847/1538-4357/834/1/17
Choi, J.-H., & Nagamine, K. 2009, MNRAS, 393, 1595, doi: 10.1111/j.1365-2966.2008.14297.x
Claret, A., & Bloemen, S. 2011, A&A, 529, A75, doi: 10.1051/0004-6361/201116451
Cumming, A., Marcy, G. W., & Butler, R. P. 1999, ApJ, 526, 890, doi: 10.1086/308020
Dressing, C. D., & Charbonneau, D. 2015, The Astrophysical Journal, 807, 45, doi: 10.1088/0004-637x/807/1/45
Endl, M., Cochran, W. D., Kürster, M., et al. 2006a, ApJ, 649, 436, doi: 10.1086/506465
—. 2006b, ApJ, 649, 436, doi: 10.1086/506465
Ercolano, B., & Clarke, C. J. 2010, MNRAS, 402, 2735, doi: 10.1111/j.1365-2966.2009.16094.x
Feinstein, A. D., Montet, B. T., Foreman-Mackey, D., et al. 2019, PASP, 131, 094502, doi: 10.1088/1538-3873/ab291c
Fischer, D. A., & Valenti, J. 2005, ApJ, 622, 1102, doi: 10.1086/428383
Forgan, D. H., Rowlands, K., Gomez, H. L., et al. 2017, MNRAS, 472, 2289, doi: 10.1093/mnras/stx2162
Fressin, F., Torres, G., Charbonneau, D., et al. 2013, ApJ, 766, 81, doi: 10.1088/0004-637X/766/2/81
Gaia Collaboration, Brown, A. G. A., Vallenari, A., et al. 2018, A&A, 616, A1, doi: 10.1051/0004-6361/201833051
Gonzalez, G., Laws, C., Tyagi, S., & Reddy, B. E. 2001, AJ, 121, 432, doi: 10.1086/318048
Guo, X., Johnson, J. A., Mann, A. W., et al. 2017, ApJ, 838, 25, doi: 10.3847/1538-4357/aa6004
Hartman, J. D., & Bakos, G. Á. 2016, Astronomy and Computing, 17, 1, doi: 10.1016/j.ascom.2016.05.006
Haworth, T. J., Ilee, J. D., Forgan, D. H., et al. 2016, PASA, 33, e053, doi: 10.1017/pasa.2016.45
Hippke, M., David, T. J., Mulders, G. D., & Heller, R. 2019, AJ, 158, 143, doi: 10.3847/1538-3881/ab3984
Hippke, M., & Heller, R. 2019, A&A, 623, A39, doi: 10.1051/0004-6361/201834672
Howard, A. W., Marcy, G. W., Bryson, S. T., et al. 2012, ApJS, 201, 15, doi: 10.1088/0067-0049/201/2/15
Johnson, J. A., Aller, K. M., Howard, A. W., & Crepp, J. R. 2010, PASP, 122, 905, doi: 10.1086/655775
Johnson, J. A., & Apps, K. 2009, ApJ, 699, 933, doi: 10.1088/0004-637X/699/2/933
Johnson, J. L., & Li, H. 2012, The Astrophysical Journal, 751, 81, doi: 10.1088/0004-637x/751/2/81
Koppelman, H., Helmi, A., & Veljanoski, J. 2018, ApJL, 860, L11, doi: 10.3847/2041-8213/aac882
Kornet, K., Bodenheimer, P., Różyczka, M., & Stepinski, T. F. 2005, A&A, 430, 1133, doi: 10.1051/0004-6361:20041692
Kovács, G., Zucker, S., & Mazeh, T. 2002, A&A, 391, 369, doi: 10.1051/0004-6361:20020802
Marcy, G., Butler, R. P., Fischer, D., et al. 2005, Progress of Theoretical Physics Supplement, 158, 24, doi: 10.1143/PTPS.158.24
Masuda, K., & Winn, J. N. 2017, AJ, 153, 187, doi: 10.3847/1538-3881/aa647c
Mayor, M., Marmier, M., Lovis, C., et al. 2011, arXiv e-prints, arXiv:1109.2497. https://arxiv.org/abs/1109.2497
McCarthy, C., & Zuckerman, B. 2004, AJ, 127, 2871, doi: 10.1086/383559
Miller, N., & Fortney, J. J. 2011, ApJL, 736, L29, doi: 10.1088/2041-8205/736/2/L29
Mortier, A., Santos, N. C., Sousa, S., et al. 2013, A&A, 551, A112, doi: 10.1051/0004-6361/201220707
Mortier, A., Santos, N. C., Sozzetti, A., et al. 2012, A&A, 543, A45, doi: 10.1051/0004-6361/201118651
Mulders, G. D., Pascucci, I., & Apai, D. 2015, ApJ, 798, 112, doi: 10.1088/0004-637X/798/2/112
Petigura, E. A., Marcy, G. W., Winn, J. N., et al. 2018, AJ, 155, 89, doi: 10.3847/1538-3881/aaa54c
Pont, F., Zucker, S., & Queloz, D. 2006, MNRAS, 373, 231, doi: 10.1111/j.1365-2966.2006.11012.x
Ricker, G. R., Winn, J. N., Vanderspek, R., et al. 2015, Journal of Astronomical Telescopes, Instruments, and Systems, 1, 014003, doi: 10.1117/1.JATIS.1.1.014003
Santerne, A., Moutou, C., Tsantaki, M., et al. 2016, A&A, 587, A64, doi: 10.1051/0004-6361/201527329
Santos, N. C., Israelian, G., & Mayor, M. 2004, A&A, 415, 1153, doi: 10.1051/0004-6361:20034469
Sharma, S., Bland-Hawthorn, J., Johnston, K. V., & Binney, J. 2011, ApJ, 730, 3, doi: 10.1088/0004-637X/730/1/3
Sozzetti, A., Torres, G., Latham, D. W., et al. 2009, ApJ, 697, 544, doi: 10.1088/0004-637X/697/1/544
Stassun, K. G., Oelkers, R. J., Pepper, J., et al. 2018, AJ, 156, 102, doi: 10.3847/1538-3881/aad050

Thorngren, D. P., Marley, M. S., & Fortney, J. J. 2019, Research Notes of the American Astronomical Society, 3, 128, doi: 10.3847/2515-5172/ab4353

Tokovinin, A., Fischer, D. A., Bonati, M., et al. 2013, PASP, 125, 1336, doi: 10.1086/674012

Tsiaras, A., Waldmann, I. P., Rocchetto, M., et al. 2016, pylightcurve: Exoplanet lightcurve model. http://ascl.net/1612.018

Udry, S., & Santos, N. C. 2007, ARA&A, 45, 397, doi: 10.1146/annurev.astro.45.051806.110529

Wang, J., Fischer, D. A., Horch, E. P., & Huang, X. 2015, ApJ, 799, 229, doi: 10.1088/0004-637X/799/2/229

Wright, J. T., Marcy, G. W., Howard, A. W., et al. 2012, ApJ, 753, 160, doi: 10.1088/0004-637X/753/2/160

Wyatt, M. C., Clarke, C. J., & Greaves, J. S. 2007, MNRAS, 380, 1737, doi: 10.1111/j.1365-2966.2007.12244.x

Yasui, C., Kobayashi, N., Tokunaga, A. T., Saito, M., & Tokoku, C. 2010, ApJL, 723, L113, doi: 10.1088/2041-8205/723/1/L113

Zechmeister, M., & Kürster, M. 2009, A&A, 496, 577, doi: 10.1051/0004-6361:200811296

Zhou, G., Bakos, G. Á., Hartman, J. D., et al. 2017, AJ, 153, 211, doi: 10.3847/1538-3881/aa674a

Zhou, G., Huang, C. X., Bakos, G. Á., et al. 2019, AJ, 158, 141, doi: 10.3847/1538-3881/ab36b5

Zink, J. K., Hardegree-Ullman, K. K., Christiansen, J. L., et al. 2020, AJ, 159, 154, doi: 10.3847/1538-3881/ab7448